



Optimization of the compositions of polyanionic sodium-ion battery cathode $\text{NaFe}_{2-x}\text{V}_x(\text{PO}_4)(\text{SO}_4)_2$

Rachid Essehli^a, Alaa Alkhateeb^b, Abdelfattah Mahmoud^c, Frédéric Boschini^c,
Hamdi Ben Yahia^b, Ruhul Amin^{a,*}, Ilias Belharouak^a

^a Energy and Transportation Science Division, Oak Ridge National Laboratory, 1 Bethel Valley Road, Oak Ridge, TN, 37830, USA

^b Qatar Environment and Energy Research Institute, Hamad Bin Khalifa University, Qatar Foundation, P.O. Box 34110, Doha, Qatar

^c GREENMAT, CESAM Research Unit, University of Liege, Chemistry Institute B6, Quartier Agora, Allée du 6 août, 13, B-4000, Liege, Belgium

HIGHLIGHTS

- Compositional optimization of vanadium doped iron based polyanion material.
- Sodium-ion battery cathode.
- Interfacial resistances and ionic diffusivity.
- In-situ powder x-ray diffraction and Mössbauer spectroscopy measurements.

ARTICLE INFO

Keywords:

NASICON
Phosphosulfate
Sodium batteries
Diffusivity
Solid solution
Kinetics
Interfaces

ABSTRACT

Sodium (Na) super ionic conductor (NASICON) polyanionic compounds have recently attracted much attention from the battery community because of their electroactive properties and reasonably high ionic conductivities, leading to their use as a cathode in sodium-ion batteries. This article describes the compositional optimizations, crystallographic evaluations, and electrochemical behavior of a new mixed NASICON polyanionic compound, $\text{NaFe}_{2-x}\text{V}_x(\text{PO}_4)(\text{SO}_4)_2$. By doping the characteristic Fe^{3+} sites of the FeO_6 octahedrons with varying amounts of V^{3+} , the electrochemical stability and charge transport in $\text{NaFe}_2(\text{PO}_4)(\text{SO}_4)_2$ were enhanced. The resulting best composition, with crystal structure $\text{NaFe}_{1.4}\text{V}_{0.6}(\text{PO}_4)(\text{SO}_4)_2$ resolved through the Rietveld method, exhibited a stable capacity compared with the other synthesized compositions. In situ powder x-ray diffraction measurements, a single-phase intercalation/deintercalation mechanism of the NASICON structure in the measured sodium concentration window was observed with no impurity phase formation. Further electrochemical assessments revealed the interfacial charge transfer kinetics to be the rate-limiting step in the sodium concentration window. Also, the measured sodium-ion diffusivity values in the range of 6×10^{-11} to $7 \times 10^{-11} \text{ cm}^2/\text{s}$ in the measured sodium concentration range. The results reported here highlight the potential of compositionally and morphologically optimized $\text{NaFe}_{1.4}\text{V}_{0.6}(\text{PO}_4)(\text{SO}_4)_2$ with higher particle surface areas as a cathode material for high-performance sodium-ion batteries.

1. Introduction

Sodium-ion batteries are very promising candidates to replace lithium-ion batteries for large-scale energy storage systems because of their cost and safety guarantees. However, several key challenges exist in identifying suitable electrode and electrolyte materials to enable high-power and -energy density with long lifespan [1–9]. To address these challenges, several sodium-transition metals-based mixed

polyanionic materials— $\text{Na}_4\text{M}_3(\text{PO}_4)_2(\text{P}_2\text{O}_7)$ [10,11], $\text{Na}_3\text{M}(\text{PO}_4)(\text{CO}_3)$ [12], $\text{Na}_2\text{MPO}_4\text{F}$ ($\text{M} = \text{Fe}, \text{Mn}, \text{Co}$ and Ni) [13], and $\text{Na}_3\text{V}_2(\text{PO}_4)_2\text{F}_{3-x}\text{O}_x$ [14] have been widely investigated over recent years. These materials are considered as potential cathode candidates for sodium-ion batteries because of their excellent electrochemical performance, favorable crystal structures, and good thermal and structural stability. In this setting, mixed polyanionic compounds containing $(\text{SO}_4)^{2-}$ have recently been reported as an attractive sodium-ion cathode material because of

* Corresponding author.

E-mail address: aminr@ornl.gov (R. Amin).

<https://doi.org/10.1016/j.jpowsour.2020.228417>

Received 27 February 2020; Received in revised form 19 May 2020; Accepted 24 May 2020

Available online 11 June 2020

0378-7753/© 2020 Elsevier B.V. All rights reserved.

the presence of the highly electronegative $(\text{SO}_4)^{2-}$ anion. Lu et al. [15] reported for the first time the preliminary electrochemical results of a new series of mixed polyanionic with an alluaudite structure, $\text{Na}_x\text{Fe}_y(\text{PO}_4)_{3-z}(\text{SO}_4)_z$ ($0 \leq z \leq 3$). These materials were synthesized by ball-milling a mixture of $\text{Na}_2\text{Fe}_3(\text{PO}_4)_3$ and $\text{Na}_{2.56}\text{Fe}_{1.72}(\text{SO}_4)_3$ in controlled (argon) atmospheres. Lu et al. demonstrated the presence of a highly electronegative $(\text{SO}_4)^{2-}$ species in the crystal structure that increased the operational voltage window from 3.19 ($z = 0$) to 3.36 ($z = 1.5$) and finally, to 3.72 V ($z = 3$) in $\text{Na}_{2.56}\text{Fe}_{1.72}(\text{SO}_4)_3$. Further investigations revealed that the origin of the elevated voltage was the inductive effect caused by the highly electronegative $(\text{SO}_4)^{2-}$ polyanion, which corroborated the overall trend of voltage enhancement in such polyanionic compounds. Additionally, Shiva et al. prepared a phosphosulfate $\text{NaFe}_2(\text{PO}_4)(\text{SO}_4)_2$ with a large amount of impurities, leading to an unusual electrochemical behavior resulting in a trend of capacity increase with cycling [16], which warranted further investigations. In this context, in the past several years, the authors' research team has focused on developing new compounds and evaluating them as positive and negative electrode materials for both lithium- and sodium-ion batteries. These materials predominantly consist of crystalline $\alpha\text{-CrPO}_4$, alluaudite, and Na super ionic conductor (NASICON) structures [3–6, 17–21].

Recently, the authors reported the synthesis and electrochemical properties of impurity-free NASICON $\text{NaFe}_2(\text{PO}_4)(\text{SO}_4)_2$ [22], showing good electrochemical activity with an average voltage of ~ 3 V. The material delivered a capacity of 89 mA h/g with 70% of the specific capacity realized (theoretical capacity = 127 mA h g^{-1} for a $2e^-$ reaction). In this material, insertion of 1.4 Na^+ ion per formula unit $\text{NaFe}_2(\text{PO}_4)(\text{SO}_4)_2$ induced a 4.6% change in the cell volume. Expanding on this work, the authors here describe the synthesis protocols, structural evaluations, and electrochemical behavior of a new mixed polyanionic compound, $\text{NaFe}_{2-x}\text{V}_x(\text{PO}_4)(\text{SO}_4)_2$ with a NASICON crystal structure as a potential cathode material for Na^+ ion batteries. The Fe^{3+} (0.645 Å) sites of the FeO_6 octahedrons at $\text{NaFe}_{2-x}\text{V}_x(\text{PO}_4)(\text{SO}_4)_2$ were doped with V^{3+} (0.64 Å) to optimize the structural and electrochemical stability as well as increase the electrical conductivity of $\text{NaFe}_2(\text{PO}_4)(\text{SO}_4)_2$. The crystal structure was resolved by the Rietveld method from the powder x-ray diffraction (PXRD) data. The oxidation state and local environment of Fe in $\text{NaFe}_2(\text{PO}_4)(\text{SO}_4)_2$ was also determined using Mössbauer spectroscopy. The electrochemical performances were examined by galvanostatic cycling and cyclic voltammetry techniques. The galvanostatic intermittent titration technique (GITT) and electrochemical impedance spectroscopy (EIS) were also employed to measure the ionic diffusivity and interfacial charge transfer kinetics of the cathode material. The stability of the NASICON structure during cycling was also confirmed by in situ PXRD experiments of $\text{NaFe}_{1.6}\text{V}_{0.4}(\text{PO}_4)(\text{SO}_4)_2$. Overall, this systematic report aims to highlight the potential of NASICON type $\text{NaFe}_{1.6}\text{V}_{0.4}(\text{PO}_4)(\text{SO}_4)_2$ as a cathode material for sodium-ion batteries.

2. Experimental

2.1. Synthesis

The $\text{NaFe}_{2-x}\text{V}_x(\text{PO}_4)(\text{SO}_4)_2$ powders ($0 \leq x \leq 2$) were synthesized via sol-gel synthesis from stoichiometric mixtures of NaNO_3 (Aldrich, $\geq 99\%$), $\text{Fe}(\text{NO}_3)_3 \cdot 9\text{H}_2\text{O}$ (Aldrich, $\geq 98\%$), NH_4VO_3 (Aldrich, $\geq 99\%$), $(\text{NH}_4)_2\text{SO}_4$ (Aldrich, $\geq 99\%$), $\text{NH}_4\text{H}_2\text{PO}_4$ (Merk, $\geq 99\%$), and citric acid (CA) $\text{C}_6\text{H}_8\text{O}_7$ (Riedel-deHaën). First, NH_4VO_3 and CA with a mole ratio of $x:2$ were dissolved in 40 ml of water to form a clear blue solution; then, $\text{Fe}(\text{NO}_3)_3 \cdot 9\text{H}_2\text{O}$ was dissolved in 20 ml of water and added to the blue solution (Solution A). The NaNO_3 , $(\text{NH}_4)_2\text{SO}_4$, and $\text{NH}_4\text{H}_2\text{PO}_4$ precursors were dissolved together in 40 ml of water (Solution B). Solution B was then added dropwise to Solution A under continuous stirring. Finally, the solutions were left to dry at 80 °C overnight. The resulting powders were pelletized, placed in alumina crucibles, and

heated in argon at 400 °C h for 12 h to decompose the precursors and release the H_2O , NH_3 , and NO_2 molecules. The $0 \leq x \leq 1.4$ samples were heated again at 500 °C h for 20 h under argon, whereas the $1.4 \leq x \leq 2$ samples were heated at 400 °C for 20 h under argon. The progress of the reactions was monitored by PXRD measurements, and the NASICON phase was observed only for the $0 \leq x \leq 1.4$ composition range.

2.2. Elemental analysis

Semiquantitative energy-dispersive x-ray spectrometry analysis was performed with a Jeol JSM-7610F scanning electron microscope. The elemental compositions based on the Na/Fe/V/P/S atomic ratios were close to $1:2-x:x:1:2$, as expected for $\text{NaFe}_{2-x}\text{V}_x(\text{PO}_4)(\text{SO}_4)_2$ ($0 \leq x \leq 1.4$).

2.3. Powder x-ray diffraction measurements

To determine the purity of the $\text{NaFe}_{2-x}\text{V}_x(\text{PO}_4)(\text{SO}_4)_2$ samples, PXRD was performed. The data were collected at room temperature over the 2θ -angular range of $10^\circ \leq 2\theta \leq 110^\circ$ with a step size of 0.01° using a Bruker D8 ADVANCE diffractometer operating with the $\text{Cu-K}\alpha$ radiation. Full pattern-matching refinements were performed using the Jana2006 program package [23]. The backgrounds were estimated by a Legendre function, and the peak shapes were described by a pseudo-Voigt function. Operando XRD measurement ($15\text{--}45^\circ$ 2θ range, 0.02° step size, and 2 s/strip step time) was performed on a Bruker D8 diffractometer with a $\text{Cu-K}\alpha$ radiation and a LYNXEYE XE-T 1D Detector (192 strips). The electrode was prepared by mixing 80% of active material with 20% of carbon black. Operando XRD data were collected during electrochemical cycling in a specially designed cell with a beryllium window, using the diffractometer and a Biologic VMP3 galvanostat. The XRD patterns were recorded every hour during the first cycle in the galvanostatic regime at C/40, which corresponds to the reaction of 0.1 Na per formula unit.

2.4. Mössbauer spectroscopy

Mössbauer spectroscopy data of the ^{57}Fe transmission were recorded with a constant-acceleration spectrometer with a $^{57}\text{Co}(\text{Rh})$ source at room temperature. The Mössbauer spectrum absorber was prepared with 40 mg/cm^2 of material mixed with boron nitride. The spectrometer was calibrated at room temperature with the magnetically split sextet spectrum of a high-purity $\alpha\text{-Fe}$ foil as the reference absorber. The measurements were carried out in the ± 4 mm/s velocity ranges. Fitting the experimental data, the spectral parameters such as isomer shift (δ), quadrupole splitting (Δ), linewidth (Γ), and relative resonance areas of the different spectral components were determined. The validity of fits was judged basis on minimizing the number of parameters and χ^2 values.

2.5. Thermal analysis

Thermogravimetric analysis (TGA) was performed on the $\text{NaFe}_{2-x}\text{V}_x(\text{PO}_4)(\text{SO}_4)_2$ ($0 \leq x \leq 2$) samples using a TA Instruments Discovery Thermogravimetric Analyzer. The measurements were conducted between 25 °C and 800 °C or 900 °C with a heating rate of 10 °C/min. The experiments were performed in platinum crucibles under argon atmosphere.

2.6. Electrochemical measurements

Positive electrodes were made from mixtures of $\text{NaFe}_{2-x}\text{V}_x(\text{PO}_4)(\text{SO}_4)_2$ ($0 \leq x \leq 1$) powders, acetylene black, and polyvinylidene fluoride in a weight ratio of 70:22:8. The resulting electrode films were cut into discs ($\phi = 14$ mm) and dried at 120 °C for 12 h under vacuum. The electrolyte was 1 M NaPF_6 dissolved in ethylene carbonate (EC), and propylene carbonate (PC) (1 M NaPF_6 in EC/PC).

Coin cells (CR2032) embedding $\text{NaFe}_{2-x}\text{V}_x(\text{PO}_4)(\text{SO}_4)_2/\text{NaPF}_6+\text{EC} + \text{PC}/\text{Na}$ were assembled in an argon-filled glove box with glass fiber (Whatman Grade GF/A, $\Phi = 20$ mm) as separators. Room-temperature galvanostatic cycling tests (constant current mode) for all the $\text{NaFe}_{2-x}\text{V}_x(\text{PO}_4)(\text{SO}_4)_2$ ($0 < x \leq 1$) electrodes were performed using an Arbin cycler in the voltage range of 1.5–4.5 V at a C/10 rate; then, the rate capability was performed for the $x = 0.4$ sample. The GITT was also applied to the $\text{NaFe}_{1.6}\text{V}_{0.4}\text{PO}_4(\text{SO}_4)_2$ active electrode material. The cell was charged/discharged galvanostatically at C/10 rate to form a stable solid electrolyte interphase layer in the first cycle. Then, a charging/discharging current equivalent to a C/30 rate was applied using Solartron 1470E battery cycler for 2 h to attain a certain state of charge/discharge (SOC/SOD), followed by a 2-h rest to reach the steady-state cell voltage. The procedure was repeated stepwise to cover whole states of charge/discharge. During this titration process, a sodium concentration gradient was built up across the active particles. Consequently, a cell voltage polarization occurred, followed by a relaxation of the cell voltage (depolarization) with time at the open-circuit voltage (OCV) condition. Then, the ionic diffusivity was derived from the voltage relaxation process as the derivative of the cell voltage depolarization vs. time. Details of the data evaluation and equations were discussed in a previous report [22]. After partial sodiation/desodiation, the cell was relaxed under the OCV condition in every step to reach the steady state in which the voltage decay was less than 2 mV/h at the end of the time interval. Thereafter, EIS was performed in the frequency range of 5 MHz to 0.5 Hz to using a sinusoidal voltage amplitude of 10 mV. The obtained EIS spectra were fitted using an equivalent circuit model built in ZView software to extract different resistive processes in the electrochemical measurements.

3. Results and discussion

3.1. Structural refinement

Following the first heat treatments at 400 °C for 12 h under argon, XRD patterns were collected; all the samples had an amorphous nature, which was determined since no XRD peak was detected. This result confirmed that 400 °C is not hot enough to crystallize this material. After the second heat treatment at 500 °C, the XRD analyses indicated that pure NASICON phases could be formed only for $0 < x \leq 1$. Full pattern-matching refinements using the space group *R*-3c and the cell parameters of $\text{NaFe}_2(\text{PO}_4)(\text{SO}_4)_2$ could index all the peaks except for the one at $2\theta = 39^\circ$ (cf. Supporting Figs. S1–S7). Therefore, the symmetry was reduced from *R*-3c to *R*-3. This symmetry enabled indexing of all the powder patterns. Evaluation of the obtained XRD data revealed the refined cell parameters listed in Table 2. A Rietveld refinement was performed for $x = 0.4$. The crystal structure of $\text{NaFe}_{1.6}\text{V}_{0.4}(\text{PO}_4)(\text{SO}_4)_2$ was solved using the structure of $\text{NaMgFe}(\text{SO}_4)_3$ as a starting structural model [30]. Statistical disorders of Fe/V and P/S were introduced, and constraints on their occupancies and atomic displacement parameters were also imposed. The Rietveld analysis of the XRD data collected at 300 K led to the reliability factors listed in Table 2 ($R_p = 0.26\%$, $R_{wp} = 0.36\%$, $R_B = 4.86\%$). The final atomic positions are given in Table 3. Fig. 1 shows a good agreement between the experimental and calculated patterns.

Table 1

Cell parameters for $\text{NaFe}_{2-x}\text{V}_x(\text{PO}_4)(\text{SO}_4)_2$ ($0 < x \leq 1$).

Composition (x)	a (Å)	c (Å)	V (Å ³)	Space group	Formula	Reference
0.0	8.4416	22.0137	1,358.57	<i>R</i> -3c	$\text{NaFe}_2(\text{PO}_4)(\text{SO}_4)_2$	Previous work [20]
0.2	8.4560 ± 0.001	22.0239 ± 0.001	1,363.84	<i>R</i> -3	$\text{NaFe}_{1.8}\text{V}_{0.2}(\text{PO}_4)(\text{SO}_4)_2$	This work
0.4	8.4215 ± 0.001	22.0524 ± 0.001	1,354.47	<i>R</i> -3	$\text{NaFe}_{1.6}\text{V}_{0.4}(\text{PO}_4)(\text{SO}_4)_2$	This work
0.6	8.4266 ± 0.001	22.0304 ± 0.001	1,354.77	<i>R</i> -3	$\text{NaFe}_{1.4}\text{V}_{0.6}(\text{PO}_4)(\text{SO}_4)_2$	This work
0.8	8.4215 ± 0.001	22.0524 ± 0.001	1,354.48	<i>R</i> -3	$\text{NaFe}_{1.2}\text{V}_{0.8}(\text{PO}_4)(\text{SO}_4)_2$	This work
1.0	8.4019 ± 0.001	22.0562 ± 0.001	1,348.40	<i>R</i> -3	$\text{NaFeV}(\text{PO}_4)(\text{SO}_4)_2$	This work

Table 2

Crystallographic data and structure refinement for $\text{NaFe}_{1.6}\text{V}_{0.4}(\text{PO}_4)(\text{SO}_4)_2$.

Rietveld refinement	
Crystal data	
Chemical formula	$\text{NaFe}_{1.6}\text{V}_{0.4}(\text{PO}_4)(\text{SO}_4)_2$
M_r	419.81
Crystal system	Trigonal
Space group	<i>R</i> -3 (No 148)
Temperature (K)	293
a (Å)	8.4215 ± 0.001,
b (Å)	8.4215 ± 0.001,
c (Å)	22.0524 ± 0.001
V (Å ³)	1354.76
Z	6
Data collection	
Diffractometer	Bruker D8 ADVANCE
Radiation type	$\text{CuK}_{\alpha 1}$ $\text{CuK}_{\alpha 2}$
2 θ_{min} , 2 θ_{step} , 2 θ_{max} values (°)	10, 0.01, 110
Refinement	
R_p	0.026
R_{wp}	0.036
R_{exp}	0.018
R(F)	0.029
R_{Bragg}	0.0486
Quality of fit χ^2	3.8
Number of data points	9785
Number of parameters	49
Profile function	Pseudo-Voigt
Background	Chebyshev function with 15 terms

Table 3

Fractional atom coordinates and isotropic atomic displacement parameters (Å²) for $\text{NaFe}_{1.6}\text{V}_{0.4}(\text{PO}_4)(\text{SO}_4)_2$ from x-ray powder diffraction data at 300 K.

Atom	Wyck.	Occ.	X	Y	Z	U _{iso} (Å ²)
Na1	3a		0	0	0	0.039(5)
Na2	3b		0	0	1/2	0.062(6)
S1/P1	18f	0.667/ 0.333	0.2919(4)	0.0017(6)	0.2508 (3)	0.0095 (3)
O1,1	18f		0.0141(7)	0.1970 (11)	0.1960 (3)	0.006(2)
O1,2	18f		−0.1785 (12)	−0.2203 (11)	0.3061 (3)	0.031(3)
O2,1	18f		0.1824(7)	0.1840(6)	0.0858 (2)	0.0099 (17)
O2,2	18f		0.0508(6)	−0.1555 (7)	0.4088 (2)	0.0121 (15)
Fe1/ V1	6c	0.8/0.2	0	0	0.1472 (2)	0.0042 (11)
Fe2/ V2	6c	0.8/0.2	0	0	0.3528 (2)	0.0190 (12)

For $x = 1.2$ and $x = 1.4$, the NASICON phases were observed; however, tiny peaks of an unidentified impurity were detected. For $x > 1.4$, the samples remained amorphous because of the low-temperature heat treatment performed. The TGA measurements demonstrated that all the samples showed around 30% of weight loss due to the release of SO₂ gas. Furthermore, their decomposition temperatures decreased with the increase of vanadium content (Fig. 2). Therefore, the $x > 1.4$ samples could not be heated above 400 °C to form NASICON phases.

SEM micro graph of $\text{NaFe}_{2-x}\text{V}_x(\text{PO}_4)(\text{SO}_4)_2$ with $x = 0.2, 0.4, 0.6, 0.8$

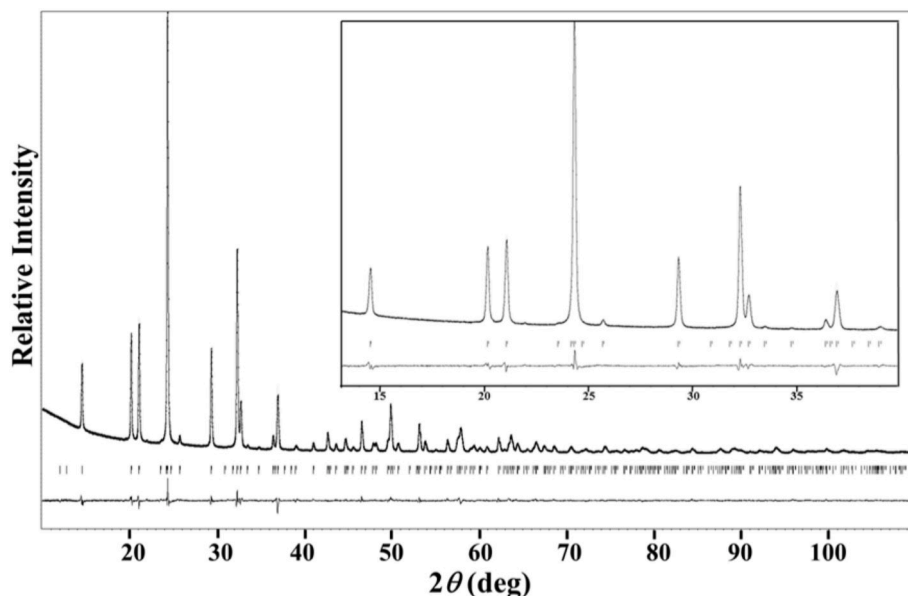


Fig. 1. Final observed, calculated, and difference plots for PXRD (Cu-K α radiation) Rietveld refinement of the NaFe_{1.6}V_{0.4}(PO₄)(SO₄)₂ powder.

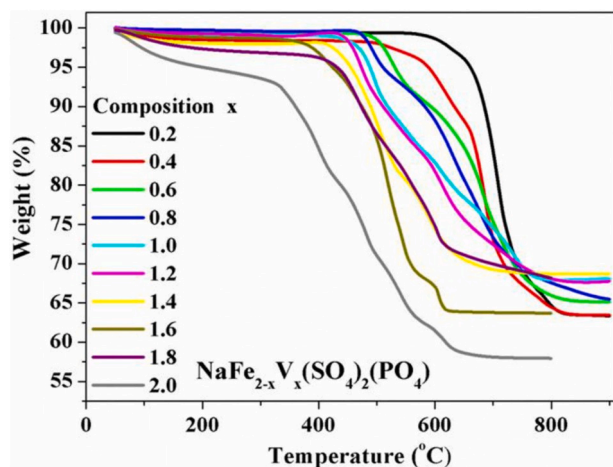


Fig. 2. TGA thermal analyses for NaFe_{2-x}V_x(PO₄)(SO₄)₂ ($0 < x \leq 2$) samples after the first heat treatment at 400 °C.

and 1.0 is given in the supporting Fig. S8 and all the samples exhibited similar micro structure. There was no specific particle shape was observed and the particles are agglomerated.

3.2. Crystal structure

The NaFe_{2-x}V_x(PO₄)(SO₄)₂ ($0 < x \leq 1$) compounds crystallized with the NASICON structure with cell parameters very similar to those of NaMgFe(SO₄)₃ [24]. The structure can be described as a covalent skeleton [(Fe/V)₂P₃O₁₂] built of Fe/VO₆ octahedra and XO₄ tetrahedra (X = S, P), which formed 3D interconnected channels with four types of interstitial positions (3a, 3b, 9d, 9e) in which sodium atoms and vacancies were distributed (Fig. 3). The interatomic distances in NaFe_{2-x}V_x(PO₄)(SO₄)₂ ($x = 0.4$) are listed in Table 4.

The FeO₆ octahedra were slightly distorted with d(Fe-O) distances ranging from 1.932 to 2.052 Å with average distances of 1.992 and 1.965 Å for Fe1 and Fe2, respectively. These values are in good agreement with the value of 1.95 Å calculated from the sum of the effective ionic radii of the six-coordinated low spin Fe³⁺ and O²⁻ [25]. The bond valence sums of 3.24 and 3.17 indicate that Fe1 and Fe2 were slightly

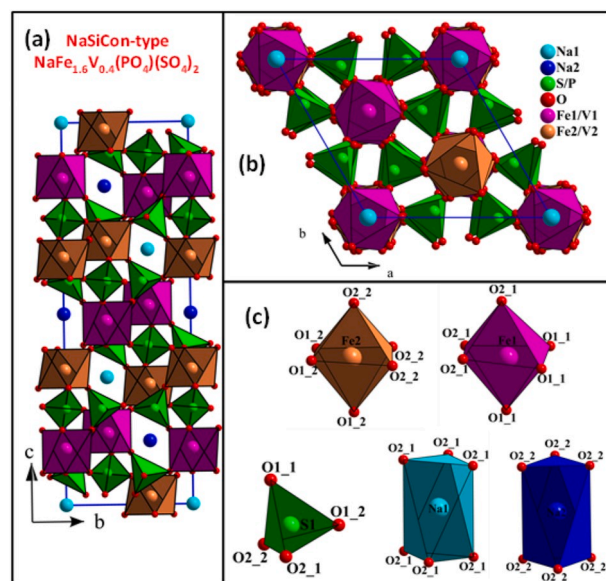


Fig. 3. Projection view of the crystal structure of NaFe_{1.6}V_{0.4}(PO₄)(SO₄)₂ (a) along the *a* axis, (b) *c* axis, and (c) coordination numbers of Na, Fe/V, and S/P atoms.

over-bonded [26,27] and the P1/S1O₄ tetrahedra were strongly distorted. The P1/S1-O distances ranged from 1.470 to 1.483 Å with an average value of 1.477 Å. This value was lower than the values 1.55 and 1.50 Å calculated from the sum of the effective ionic radii of the four-coordinated P⁵⁺, S⁶⁺, and O²⁻. The bond valence sums of 5.84 and 5.95 for P1 and S1, respectively, indicate that P1 was over-bonded.

The Na1⁺ and Na2⁺ cations were surrounded by six oxygen atoms (Fig. 3c). The average Na1-O distance of 2.441 Å was consistent with the value of 2.42 Å calculated from the sum of the effective ionic radii of the four-coordinated Na⁺ and O²⁻ [25], whereas the average Na2-O distance of 2.551 Å was larger. The bond valence sums of 1.07 and 0.795 for Na1 and Na2, respectively, indicate that Na2 was slightly under-bonded.

Table 4
Interatomic distances (Å) and bond valences of NaFe_{1.6}V_{0.4}(PO₄)(SO₄)₂.

	Distances
Na1-O2_1 (× 6)	2.441(5)
Na1 ⁺	1.070 [6] ^a
Na2-O2_2 (× 6)	2.551(6)
Na2 ⁺	0.795 [6] ^a
S1/P1-O1_1	1.483(10)
S1/P1-O1_2	1.472(11)
S1/P1-O2_1	1.470(5)
S1/P1-O2_2	1.483(8)
	<1.477>
P1 ⁺⁵ /S1 ⁺⁶	5.84/5.95 [4] ^a
Fe1/V1-O2_1 (× 3)	2.052(7)
Fe1/V1-O1_1 (× 3)	1.932(9)
	<1.992>
Fe1 ³⁺ /V1 ³⁺	3.24/3.10 [6] ^a
Fe2/V2-O1_2 (× 3)	1.993(7)
Fe2/V2-O2_2 (× 3)	1.996(6)
	<1.965>
Fe2 ³⁺ /V2 ³⁺	3.17/3.04 [6] ^a

Average distances are given in < > and coordination numbers are given in [].

^a Bond valence sum. Bond valence = $e^{(r_0-r)/b}$ with the following parameters: $b = 0.37$, r_0 (Na^I-O) = 1.803, r_0 (Fe^{III}-O) = 1.759, r_0 (V^{III}-O) = 1.743, r_0 (S^{VI}-O) = 1.624 and r_0 (P^V-O) = 1.617 Å [26,27].

3.3. Mössbauer spectroscopy

Mössbauer spectroscopy is an excellent technique for probing the oxidation states and the local environment of Fe atoms in Fe-based phosphate materials. To investigate the oxidation state and the local environment of Fe in the NaFe_{1.6}V_{0.4}(PO₄)(SO₄)₂ material, ⁵⁷Fe Mössbauer spectroscopy was used. The spectrum was consistent with the presence of paramagnetic Fe, confirming the paramagnetic behavior of the material at room temperature. The lack of magnetic ordering also proved the absence of magnetic Fe oxides-based impurities at the 1 Fe at. % level, in good agreement with XRD results, which confirms the high purity of the sample.

The Mössbauer spectrum of the NaFe_{1.6}V_{0.4}(PO₄)(SO₄)₂ sample recorded at room temperature (Fig. 4) shows the presence of two Fe(III) sites and two Fe(II) sites. A high-quality fit of the NaFe_{1.6}V_{0.4}(PO₄)(SO₄)₂ spectrum was obtained using four components corresponding to two Fe(III) doublets (red and brown lines) that represent 86% of the total Fe and two Fe(II)-doublets (blue and purple lines). These data are in

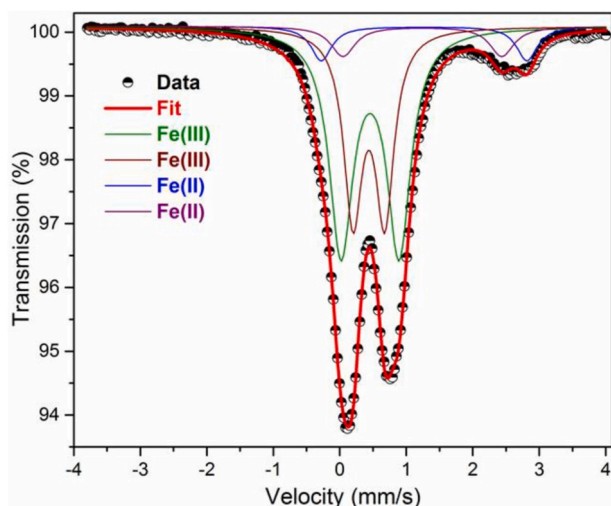


Fig. 4. Mössbauer spectrum of the NaFe_{1.6}V_{0.4}(PO₄)(SO₄)₂PO₄ material.

good agreement with the XRD data that suggests that the NaFe_{1.6}V_{0.4}(PO₄)(SO₄)₂ phase has four Fe crystallographic sites or some structural defects. The hyperfine parameters are presented in the Table 5.

The prepared phase was also determined to be pure. The two Fe(III) doublets have isomer shifts of around 0.44 mm/s but with different quadrupole splitting of 0.87 mm/s and 0.47 mm/s, confirming the different local environments of two Fe(III) sites corresponding to distorted octahedral sites. The estimated average isomer shift and quadrupole splitting of Fe(III) were consistent with six-fold coordination, whereas Fe(II) sites showed broad quadrupole doublets (3.09 and 2.39 mm/s) with isomer shifts of about 1.26 mm/s and 1.24 mm/s. These results confirm that Fe(II)-ions were in a highly asymmetric environment in the structure of the NaFe_{1.6}V_{0.4}(SO₄)₂PO₄ material compared with Fe(III)-ions. The Mössbauer spectrum of the NaFe_{1.6}V_{0.4}(PO₄)(SO₄)₂ sample recorded at room temperature (Fig. 4) shows the presence of two Fe(III) sites and two Fe(II) sites. A high-quality fit of the NaFe_{1.6}V_{0.4}(PO₄)(SO₄)₂ spectrum was obtained using four components corresponding to two Fe(III) doublets (green and brown lines) that represent 86% of the total Fe and two Fe(II)-doublets (blue and purple lines) and there red line correspond to fit.

3.4. Electrochemical properties

3.4.1. Galvanostatic cycling

The effect of vanadium-doping on the electrochemical performance of the NaFe_{2-x}V_x(PO₄)(SO₄)₂ samples was examined by performing galvanostatic charge/discharge measurements. Fig. 5a shows the charge/discharge profiles of the NaFe_{2-x}V_x(PO₄)(SO₄)₂ samples at 0.1 C in the voltage window of 1.5–4.5 V vs. Na⁺/Na. The average working potential of the cathode was ~3 V, with charge/discharge curves exhibiting similar behavior to that of NASICON NaFe₂(PO₄)(SO₄)₂ [23]. The NaFe_{2-x}V_x(PO₄)(SO₄)₂ with x = 0.2, 0.4, and 0.6 samples showed a relatively high discharge capacity (over 72 mAhg⁻¹) with a capacity retention of 96% after 50 cycles. The NaFe_{1.6}V_{0.4}(PO₄)(SO₄)₂ composition exhibited comparatively better cycling stability compared with the other compositions. The cell polarization trend with an increasing rate during discharge/charge cycling for NaFe_{1.6}V_{0.4}(PO₄)(SO₄)₂ is shown in Fig. 6a at rates 0.1–5C. The rate performance was also tested from 0.1 to 10C (Fig. 6b). The capacity obtained at the rate of 0.1C was observed to recover after returning from 10 to 0.1C. This observation revealed that rate performance of the samples was limited by either interfacial kinetics at the electrode/electrolyte interface or by charge transport properties of active particles. Details are discussed later in this paper at section 3.4.2.

To further investigate the sodium intercalation/deintercalation mechanism into/from the host structure, operando XRD analysis was conducted with the specific Swagelok electrochemical cell in reflection mode during the discharge/charge process as shown in Fig. 7. During the discharge, only a slight shifting of peaks was observed (Fig. 7) without the formation of any new phase, indicating a single-phase mode of deintercalation in NaFe_{1.6}V_{0.4}(PO₄)(SO₄)₂. A complete original pattern was retrieved at 1.5 V, indicating the reversible nature of the intercalation process.

The in situ analysis clearly confirmed that during the charging/discharging, the sodium intercalation/deintercalation in NaFe_{1.6}V_{0.4}(PO₄)

Table 5
Hyperfine parameters of the room-temperature Mössbauer spectra of the NaFe_{1.6}V_{0.4}(SO₄)₂PO₄ material.

	δ (mm s ⁻¹)	Δ (mm s ⁻¹)	Γ (mm s ⁻¹)	Area (%)
Fe(III)	0.45 (1)	0.87 (1)	0.43 (1)	52 (1)
Fe(III)	0.43 (1)	0.47 (2)	0.34 (1)	34 (1)
Fe(II)	1.26 (1)	3.09 (1)	0.38 (1)	7 (1)
Fe(II)	1.24 (1)	2.39 (2)	0.43 (1)	7 (1)

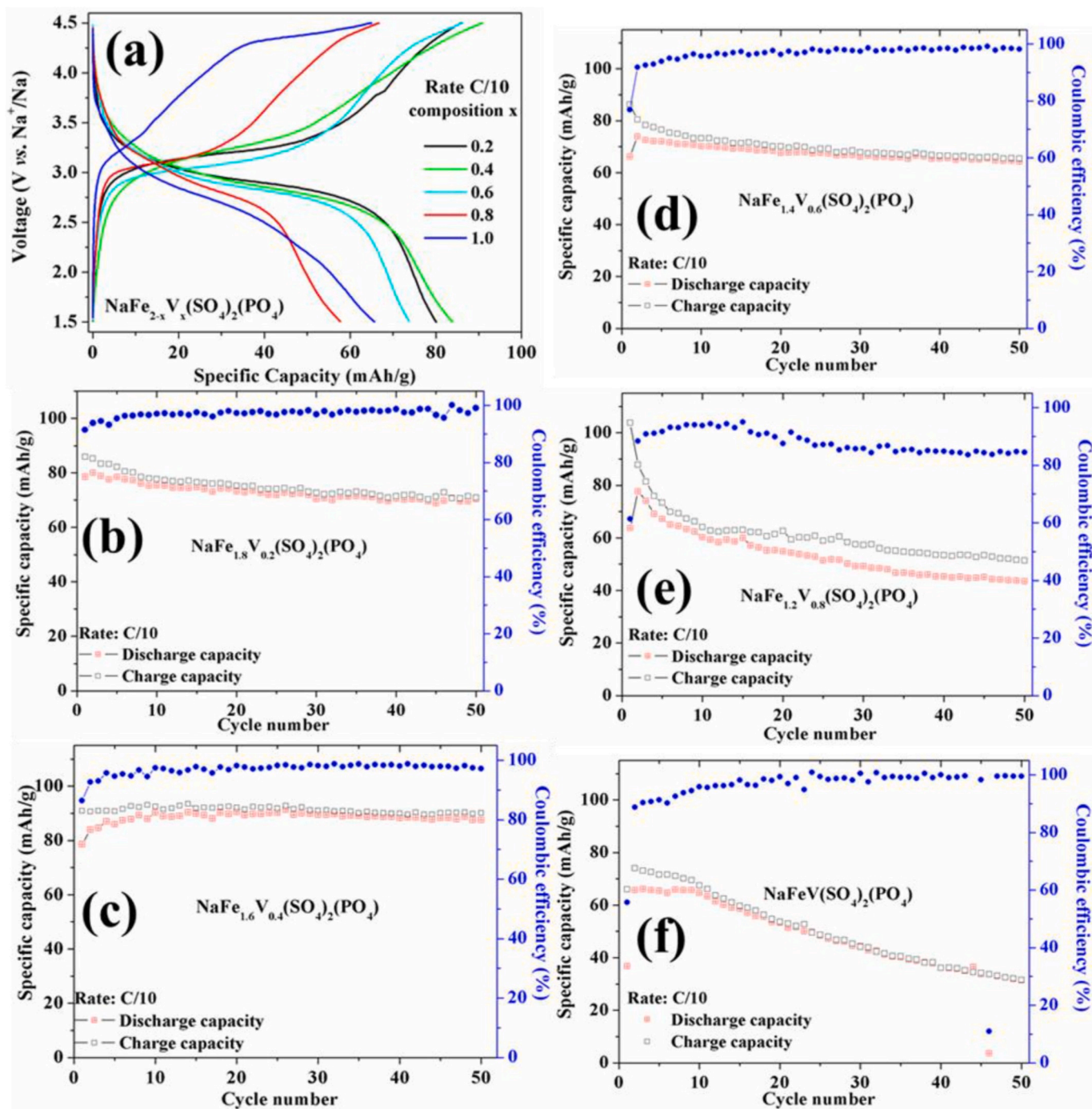


Fig. 5. (a) Charge/discharge curves of the second cycles recorded at room temperature in a CC mode at the rate of C/10 in the voltage range of 1.5–4.5 V vs. Na⁺/Na, and capacity retention for NaFe_{2-x}V_x(PO₄)(SO₄)₂ where (b) x = 0.2, (c) x = 0.4, (d) x = 0.6, (e) x = 0.8, and (f) x = 1 (1e⁻ reaction delivers a specific capacity of ~64 mA h/g).

(SO₄)₂ occurred through a reversible single-phase reaction rather than a two-phase reaction. The peak shifts corresponded to the slight variations of the lattice parameters with the amount of inserted Na⁺.

3.4.2. Interfacial charge transfer resistance and sodium-ion diffusivity

The GITT was applied to the best composition of NaFe_{1.6}V_{0.4}(PO₄)(SO₄)₂ to measure the interfacial charge transfer resistance at electrolyte/electrode interfaces. The GITT curves of the charge/discharge processes are displayed in Fig. 8a as a function of time.

The NaFe_{1.6}V_{0.4}(PO₄)(SO₄)₂ vs. Na/Na⁺ cell was first discharged stepwise down to 1.5 V to convert the NaFe_{1.6}V_{0.4}(PO₄)(SO₄)₂ into a

reduced phase (Fe³⁺ to Fe²⁺), followed by charging again to 4.5 V. Fig. 8a shows that the NaFe_{1.6}V_{0.4}(PO₄)(SO₄)₂ material exhibited a single-phase sodiation/desodiation mechanism in the measured voltage window (1.5–4.5 V). Fig. 8b shows the EIS spectra recorded on the half-cell of the NaFe_{1.6}V_{0.4}(PO₄)(SO₄)₂ material in the charging states. The cell was held at the OCV for 2 h with a voltage decay rate of ~3 mV/h at the end of the partial desodiation. Under the OCV condition, the cell voltage at a particular SOC/SOD was in between the oxidation and reduction states. Notably, small bias potentials during the EIS measurements in such a situation can initiate partial sodium intercalation/deintercalation. The measured Nyquist plots of NaFe_{1.6}V_{0.4}(PO₄)(SO₄)₂

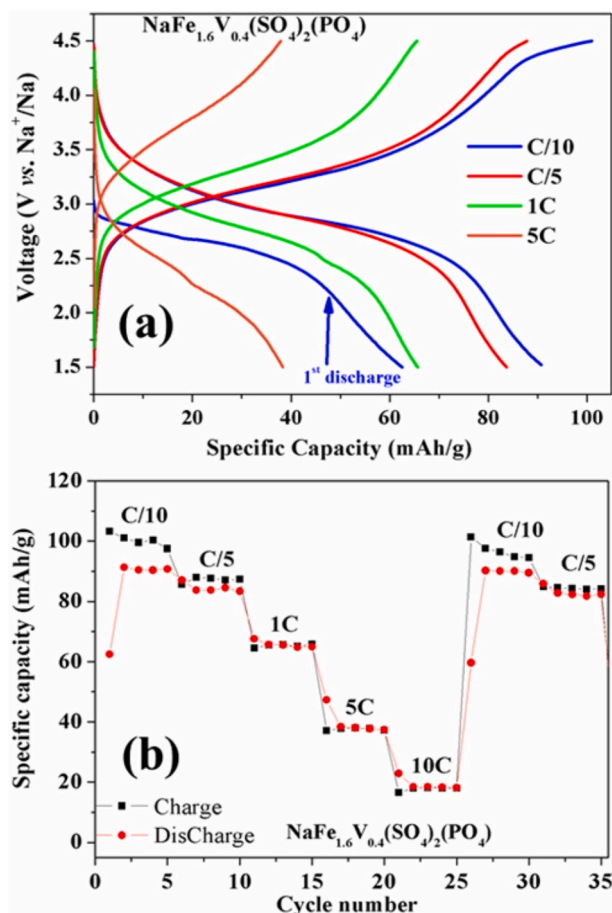


Fig. 6. (a) Charge/discharge curves of NaFe_{1.6}V_{0.4}(PO₄)(SO₄)₂ recorded at room temperature in a CC mode at the rate of C/10, C/5, 1C, and 5C in the voltage range of 1.5–4.5 V vs. Na⁺/Na, and (b) the rate capability.

comprises the following features:

1. At high frequencies, Ohmic contribution caused by the ionic resistance of the electrolyte solution (R1)—along with a minor contribution of the solid electrolyte interphase and inductive effect—appeared below the real axis (L1). Induction was directly proportional to frequency ($L \propto f$).
2. A single semicircle was observed at medium-high frequencies, which was likely due to the charge transfer resistance (R2) at the NaFe_{1.6}V_{0.4}(PO₄)(SO₄)₂/electrolyte interface, since the associated capacitance value was relatively high (10^{-6} F). The separation of charge transfer resistance at the metallic sodium/electrolyte interface was troublesome since it appeared to overlap with the relaxation process of the cathode interface.
3. A Warburg response (Ws) appeared at low frequencies. Very similar impedance spectra were measured during the discharge process.

Different resistance processes were separated by fitting the spectra using the equivalent circuit shown in the top of Fig. 8b, and the obtained data for the semicircle are displayed in Fig. 8c as a function of the SOC/SOD along with the electrolyte Ohmic resistance (R1). Fig. 8c shows that the resistances of the semicircles gradually increased and decreased with the degree of sodiation/desodiation, respectively, whereas R1 remained almost constant with the various SOC and SOD. The charge transfer reaction associated at the sodium/electrolyte interface might not have varied with the SOC or SOD. Here, R2 was mainly associated with the NaFe_{1.6}V_{0.4}(PO₄)(SO₄)₂/electrolyte interface since the formation of mixed valence Fe²⁺/Fe³⁺ significantly affected the NaFe_{1.6}V_{0.4}(PO₄)

(SO₄)₂/electrolyte interface during the desodiation/sodiation process.

Fig. 8c also shows that the resistance R2 was relatively high. This huge value of R2 was likely due to agglomerated particle morphology and a relatively small surface area exposed to the electrolyte. The EIS results imply that the interfacial charge transfer resistance was likely rate-limiting in the whole range of sodium concentrations.

The voltages obtained during the depolarization of the cell at different SOC and SOD were fitted with Eq. (1) to derive the relaxation time, τ .

$$\ln(U(t) - U_{(t=\infty)}) = \ln A - \frac{t}{\tau} \quad (1)$$

A is the constant term for a particular material, and $U(t)$ and $U_{(t=\infty)}$ are the cell voltage at times (t) and $t = \infty$. The slope of the plot, $\ln(U(t) - U_{(t=\infty)})$ vs. t , provides the relaxation time, τ . Details about the equation and its use and data evaluation can be found in the references. [28–30] As described in Section 2, depolarization was caused by the development of a sodium concentration gradient across the active particle during the titration process. After each desodiation/sodiation step, the cell was allowed to relax under the OCV condition, leading to steady-state cell voltage. As an example, the depolarization cell voltage can be well-fitted with Eq. (1) (Fig. S8a). The relaxation time obtained from the fitted data is displayed in Fig. 8d as a function of SOC/SOD, which shows that relaxation time gradually decreased up to 75% SOC. Thereafter, a gradual increase was observed with further desodiation. Because getting the accurate particle diameter is difficult, the authors could not reliably calculate the diffusivity values of the material. Nevertheless, the obtained relaxation times clearly indicated the range and trend of diffusivity as a function of sodium concentration. The diffusivity values were between 6×10^{-11} and 7×10^{-11} cm²/s (Fig. S8b) in the measured sodium concentration window by assuming a 2 μ m diffusion length obtained from the SEM micrographs. Therefore, diffusivity can also be a rate-limiting factor at higher cycling rates as shown in Fig. 6b.

4. Conclusions

Several new mixed polyanionic NaFe_{2-x}V_x(PO₄)(SO₄)₂ ($x = 0.2, 0.4, 0.60, 0.8$, and 1.0) samples were synthesized with optimized compositions, considering structural stability and electrochemical performances. The structural stability was investigated by XRD followed by Rietveld refinement protocols to obtain accurate structural refinements of the synthesized compounds. The obtained parameters as a result of solving the crystal structure indicated NASICON phases for these materials. Of the various compositions evaluated, the NaFe_{1.6}V_{0.4}(PO₄)(SO₄)₂ composition exhibited comparatively better electrochemical performance. The structural stability was also investigated as a function of sodium content by using in situ XRD measurements during the galvanostatic charge/discharge process. The in situ analysis confirmed that the sodium intercalation/deintercalation in the NaFe_{1.6}V_{0.4}(PO₄)(SO₄)₂ occurred through a reversible single-phase reaction instead of the prevailing notion of a two-phase reaction. However, XRD data suggested that the NaFe_{2-x}V_x(PO₄)(SO₄)₂ phase has two Fe crystallographic sites or some structural defects, which agrees with spectra obtained from Mössbauer measurements. The results from Mössbauer studies also confirmed that the Fe (II)-ions are in a highly asymmetric environment in the structure of the NaFe_{1.6}V_{0.4}(SO₄)₂PO₄ compared with Fe (III)-ions. Further investigating the electrochemical behavior using EIS measurements indicated that the electrochemical performances of these materials were limited by interfacial charge transfer kinetics in the whole range of sodium concentration at practical C rates. The range of diffusivity values determined using GITT measurements did not show significant variation and was between 6×10^{-11} and 7×10^{-11} cm²s⁻¹ in the measured sodium concentration window. At higher C rates with particle sizes larger than 4 μ m, ionic diffusivity appeared to also be a key rate-limiting factor. Overall, through these systematic investigations

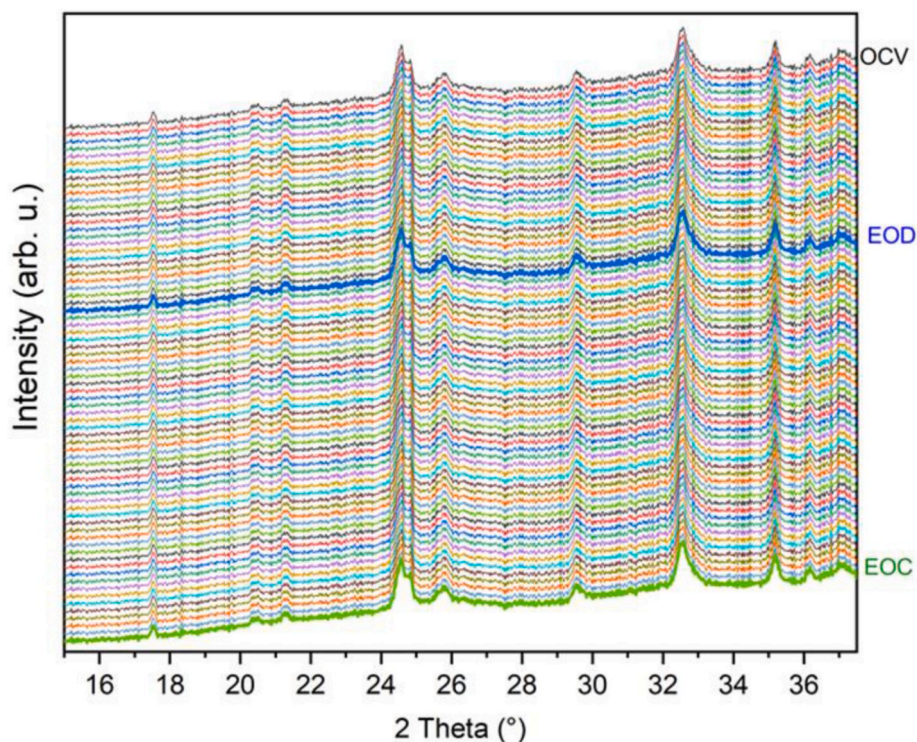


Fig. 7. Operando XRD patterns of $\text{NaFe}_{1.6}\text{V}_{0.4}(\text{PO}_4)(\text{SO}_4)_2$ collected at a rate of C/30 during the first discharge/charge cycle every 1 h in the voltage range of 1.5–4.5 V.

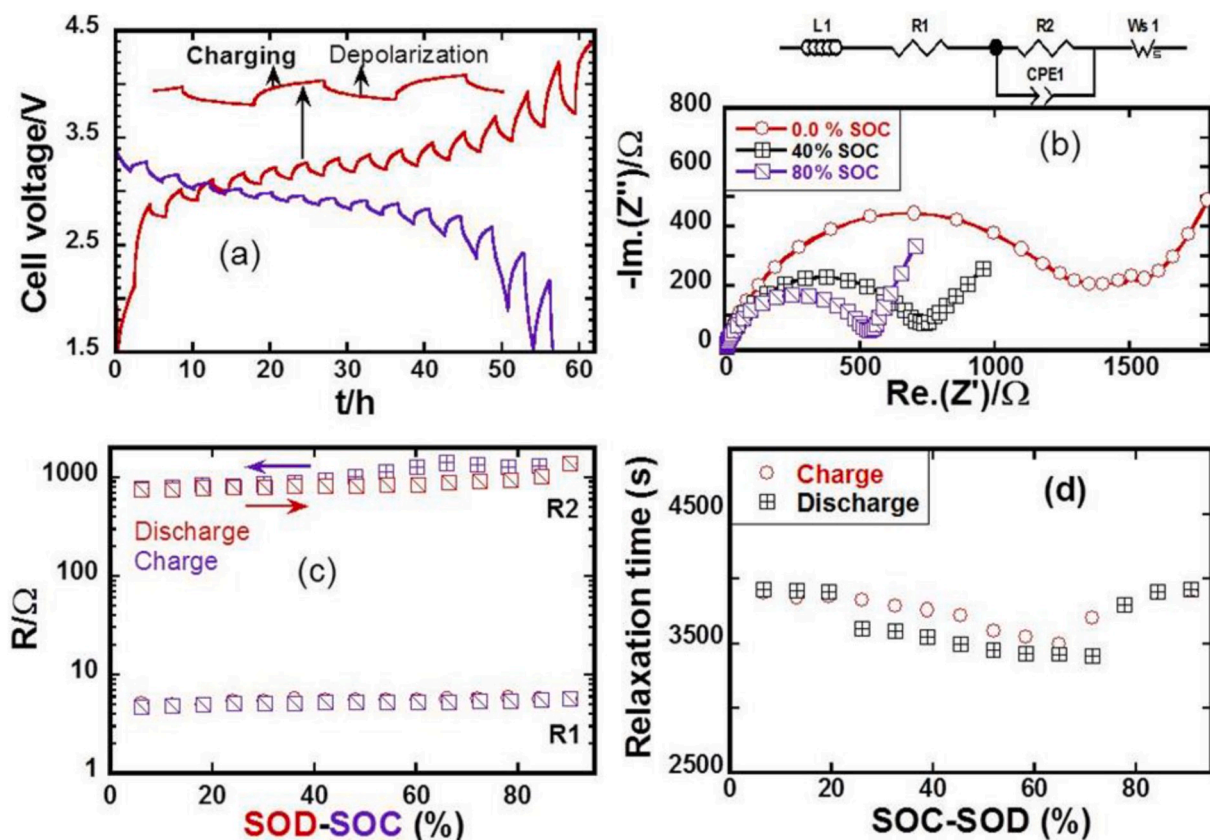


Fig. 8. (a) GITT curve measured during stepwise charge/discharge process. (b) Impedance spectra of a half-cell configuration ($\text{NaFe}_{1.6}\text{V}_{0.4}(\text{PO}_4)(\text{SO}_4)_2$ vs. Na^+/Na) at different states of discharge. (c) Resistance of different processes as a function of state of charge/discharge (SOC/SOD); the arrow indicates the trend of resistance with the degree of sodiation/desodiation. (d) Relaxation time extracted from the cell voltage depolarization.

optimizing synthesis, crystallographic, and electrochemical parameters, $\text{NaFe}_{1.6}\text{V}_{0.4}(\text{SO}_4)_2\text{PO}_4$ shows great promise for potential use as a cathode material for sodium-ion batteries.

Declaration of competing interest

The authors declare that they have no known competing financial interests or personal relationships that could have appeared to influence the work reported in this paper.

CRediT authorship contribution statement

Rachid Essehli: Conceptualization, Writing - review & editing. **Alaa Alkhateeb:** Formal analysis. **Abdelfattah Mahmoud:** Data curation. **Frédéric Boschini:** Data curation. **Hamdi Ben Yahia:** Data curation. **Ruhul Amin:** Conceptualization, Writing - review & editing. **Ilias Belharouak:** Supervision, Writing - review & editing.

Acknowledgments

This work is supported by the U.S. Department of Energy, Office of Energy Efficiency and Renewable Energy Vehicle Technology Office, under contract number DE-AC05-00OR22725.

Appendix A. Supplementary data

Supplementary data to this article can be found online at <https://doi.org/10.1016/j.jpowsour.2020.228417>.

References

- [1] B.L. Ellis, W.R.M. Makahnouk, W.N. Rowan-Weetaluktuk, D.H. Ryan, L.F. Nazar, *Chem. Mater.* 22 (2010) 1059–1070.
- [2] M.M. Rahman, I. Sultana, S. Mateti, J. Liu, N. Sharma, Y. Chen, *J. Mater. Chem.* 5 (2017) 16616–16621.
- [3] R. Essehli, I. Belharouak, H. Ben Yahia, K. Maher, A. Abouimrane, B. Orayech, S. Calder, X.L. Zhou, Z. Zhou, Y.-K. Sun, *Dalton Trans.* 44 (2015) 7881–7886.
- [4] H. Ben Yahia, R. Essehli, M. Avdeev, J.-B. Park, Y.-K. Sun, M.A. Al-Maadeed, I. Belharouak, *J. Solid State Chem.* 238 (2016) 103.
- [5] H. Ben Yahia, M. Shikano, M. Tabuchi, I. Belharouak, *Inorg. Chem.* 55 (2016) 4643.
- [6] R. Essehli, I. Belharouak, H. Ben Yahia, R. Chamoun, B. Orayech, B. El Bali, K. Bouziane, X. Zhou, Z. Zhen, *Dalton Trans.* 44 (2015) 4526–4532.
- [7] R. Essehli, H. Ben Yahia, K. Maher, M.T. Sougrati, A. Abouimrane, J.-B. Park, Y.-K. Sun, M.A. Al-Maadeed, I. Belharouak, *J. Power Sources* 324 (2016) 657–664.
- [8] M. Wen, X. Liu, Y. Zhao, S. Liu, H. Liu, Y. Dong, Q. Kuang, Q. Fan, *Int. J. Electrochem. Sci.* 12 (2017) 3153–3165, <https://doi.org/10.20964/2017.04.35>.
- [9] K. Trad, D. Carlier, L. Croguennec, A. Wattiaux, B. Lajmi, M. Ben Amara, C. Delmas, *J. Phys. Chem. C* 114 (2010) 10034–10044, <https://doi.org/10.1021/jp100751b>.
- [10] H. Kim, I. Park, D.-H. Seo, S. Lee, S.-W. Kim, W.J. Kwon, Y.-U. Park, C.S. Kim, S. Jeon, *J. Am. Chem. Soc.* 134 (2012) 10369–10372.
- [11] H. Kim, G. Yoon, I. Park, K.-Y. Park, B. Lee, J. Kim, Y.-U. Park, S.-K. Jung, H.-D. Lim, D. Ahn, S. Lee, K. Kang, *Energy Environ. Sci.* 8 (2015) 3325–3335.
- [12] H. Chen, Q. Hao, O. Zivkovic, G. Hautier, L.-S. Du, Y. Tang, Y.-Y. Hu, X. Ma, C. P. Grey, G. Ceder, *Chem. Mater.* 25 (2013) 2777–2786.
- [13] W. Huang, J. Zhou, B. Li, J. Ma, S. Tao, D. Xia, W. Chu, Z. Wu, *Sci. Rep.* 4 (2014) 4188, 1–8.
- [14] T. Ramireddy, M.M. Rahman, N. Sharma, A.M. Glushenkov, Y. Chen, *J. Power Sources* 271 (2014) 497–503.
- [15] Jiechen Lu, Shin-ichi Nishimura, Atsuo Yamada, *Chem. Mater.* 29 (8) (2017) 3597–3602, 2017.
- [16] K. Shiva, P. Singh, W. Zhou, J.B. Goodenough, *Energy Environ. Sci.* 9 (2016) 3103–3106.
- [17] R. Essehli, B. El Bali, A. Faik, S. Benmokhtar, B. Manoun, Y. Zhang, X.J. Zhang, Z. Zhou, H. Fuess, *J. Alloys Compd.* 530 (2012) 178, 0.
- [18] R. Essehli, B. El Bali, S. Ben Mokhtar, K. Bouziane, B. Manoun, M.A. Abdalslam, H. Ehrenberg, *J. Alloys Compd.* 509 (2011) 1163.
- [19] R. Essehli, B. El Bali, A. Faik, M. Naji, S. Benmokhtar, Y.R. Zhong, L.W. Su, Z. Zhou, J. Kim, K. Kang, M. Dusek, *J. Alloys Compd.* 585 (2014) 434, 0.
- [20] U. Nisar, R. Shakoor, R. Essehli, R. Amin, B. Orayech, Z. Ahmad, P.R. Kumar, R. Kahraman, S. Al-Qaradawi, A. Soliman, *Electrochim. Acta* 292 (2018) 98–106.
- [21] P.R. Kumar, A. Kheireddine, U. Nisar, R.A. Shakoor, R. Essehli, R. Amin, I. Belharouak, *J. Power Sources* 429 (2019) 149–155.
- [22] H. Ben Yahia, R. Essehli, R. Amin, K. Boulahya, T. Okumura, I. Belharouak, *J. Power Sources* 382 (2018) 144–151.
- [23] V. Petricek, M. Dusek, L. Palatinus, in: *Crystallographic Computing System JANA2006* 229, 2006, pp. 345–352.
- [24] P.R. Slater, C. Greaves, *J. Mater. Chem.* 4 (1994) 1469–1473.
- [25] R.D. Shannon, *Acta Crystallogr.* A32 (1976) 751–767.
- [26] I.D. Brown, D. Altermatt, *Acta Crystallogr.* B41 (1985) 244–247.
- [27] N.E. Brese, M. O'Keeffe, *Acta Crystallogr.* B47 (1991) 192–197.
- [28] R. Amin, I. Belharouak, *J. Power Sources* 348 (2017) 318–325.
- [29] J. Maier, *Physical Chemistry of Ionic Materials: Ions and Electrons in Solids*, Wiley, Chichester, 2004.
- [30] R. Amin, Y.-M. Chiang, *J. Electrochem. Soc.* 163 (2016) A1512–A1517.